UNITED STATES PATENT AND TRADEMARK OFFICE

BEFORE THE PATENT TRIAL AND APPEAL BOARD

3D Systems Corporation et al.,

Petitioner

v.

Intrepid Automation, Inc.,
Patent Owner.

Inter Partes Review (IPR) Proceeding Number: 2025-01241
U.S. Patent No. 11,014,301

Exhibit Number: **Exhibit 1027 for Petitioner**

Exhibit Title: Y. Chen *et al.*, "Smooth Surface Fabrication Based on Controlled Meniscus and Cure Depth in Microstereolithography," *Journal of Micro- and Nano-Manufacturing*, Vol. 3, September 2015

Date of Filing: July 8, 2025

Filed By: Petitioner 3D Systems Corporation et al.,

Description of Exhibit: A printed publication cited as prior art in the Petition for Inter Partes Review, demonstrating the anticipation of claims 1- 20 of U.S. Patent No. 11,014,301

Smooth Surface Fabrication Based on Controlled Meniscus and Cure Depth in Microstereolithography

Yayue Pan
Department of Mechanical and Industrial Engineering,
University of Illinois at Chicago,
Chicago, IL 60607

Yong Chen[1]
Epstein Department of Industrial and Systems Engineering,
University of Southern California,
Los Angeles, CA 90089
e-mail: yongchen@usc.edu

In the layer-based additive manufacturing (AM) processes, a three-dimensional (3D) model is converted into a set of two-dimensional (2D) layers. Due to such conversion, one of the major problems in the layer-based AM processes is the poor surface finish associated with the layer-based stair-stepping effect. However, the surface finish is critical for various microscale applications such as micro-optics and microfluidics. The adoption of AM technologies as a means for fabricating end-use microcomponents and tooling has been limited by such poor surface finish. The aim of this research work is to apply the state-of-the-art meniscus approach and controlled cure depth planning in the mask image projection-based microstereolithography (MIP-μSL) process to address its surface finish challenge. Mathematical models of meniscus shapes and cure depths are developed for the MIP-μSL process. Related process parameters including the minimum meniscus points, sliced layer shapes for forming meniscus, grayscale image values, and Z offsetting values are optimized to achieve the minimum approximation errors between a built part and a given nominal geometric model. A set of test cases with various curved surfaces are designed to test the developed smooth surface fabrication method. The experimental results verify the effectiveness of the proposed methods for the MIP-μSL process. [DOI: 10.1115/1.4030661]

Keywords: surface finish, additive manufacturing, meniscus, cure depth, microstereolithography, micro-optics, microfluidics

1 Introduction

The layer-based microstereolithography (μSL) technology can fabricate complicated 3D microstructures with high-aspect ratios [1–5]. During the μSL process, a given 3D model is first sliced into a set of 2D layers. By stacking the 2D layers together, a physical part can be fabricated to approximate the original computer-aided design (CAD) model. However, one of the major problems in the μSL process is the poor surface finish associated with the layer-based stair-stepping effect. Due to the use of 2D layers, the fabricated surfaces especially the ones whose normals are close to the building direction (Z axis) will have big approximation errors. Such poor surface quality limits the use of μSL in any applications that require smooth surfaces, e.g., micro-optics and microfluidics.

In the paper, we present our smooth surface fabrication method in the MIP-μSL system as illustrated in Fig. 1(*a*), while the presented approach could be adapted to any other vat photopolymerization systems, including scanning-based μSL processes. In addition, we will focus on the bottom-up projection approach while the method can also be used in the top-down projection-based systems.

Based on the building direction (i.e., Z axis) and the normal N of each surface in a CAD model, all the part surfaces can be classified into: (1) vertical surfaces ($N \cdot Z \approx 0$), (2) up-facing surfaces ($N \cdot Z > 0$), and (3) down-facing surfaces ($N \cdot Z < 0$). There is no need to specially consider the vertical surfaces since they generally do not contribute to the stair-stepping effect. Therefore, in this paper, we will focus on achieving smooth surface for the latter two cases.

1.1 Up-Facing Surface. Since the approximation error depends on the layer thickness used in the slicing of a 3D model, a dominant approach for improving the smoothness of up-facing surfaces is to reduce the layer thickness. For example, the layer thickness typically used in a microstereolithography system is 25 μm, while the layer thickness can be as small as 5 μm [6]. Even with such ultrathin layer, the fabricated up-facing surfaces still have obvious staircase effect under microscope. Recently, Gandhi and Bhole [7] presented a "bulk lithography" process for fabricating microstructures including microlens. However, the method is limited to a single layer fabrication, which limits the complexity of the built microstructures.

In our previous research [8], we developed a meniscus method to fabricate smooth up-facing surface in the top-down projection-based macroscale SL system. As shown in Fig. 1(*b*), the key idea of the meniscus approach is to closely match the fluid interfaces at the corners of intersecting planes to the related curved surfaces in the input geometry. Hence, liquid meniscuses will be formed at the corners when the cured layers emerge from the liquid. By controlling the meniscus shape and selectively curing the meniscus area, we are able to closely match the designed up-facing curvature. The work [8] demonstrated the effectiveness of the meniscus method in addressing staircase effect in most macroscale up-facing surfaces. However, due to the use of the top-down projection-based SL approach, one limitation is that the resin residual of some closed concave features (e.g., a bowl) cannot be removed; consequently, the meniscus wetting cannot be formed. In addition, microstructures features have not been studied in our previous work. In this paper, we extend the meniscus wetting

[1]Corresponding author.

Contributed by the Manufacturing Engineering Division of ASME for publication in the Journal of Micro- and Nano-Manufacturing. Manuscript received October 8, 2014; final manuscript received May 8, 2015; published online June 18, 2015. Assoc. Editor: Liwei Lin.

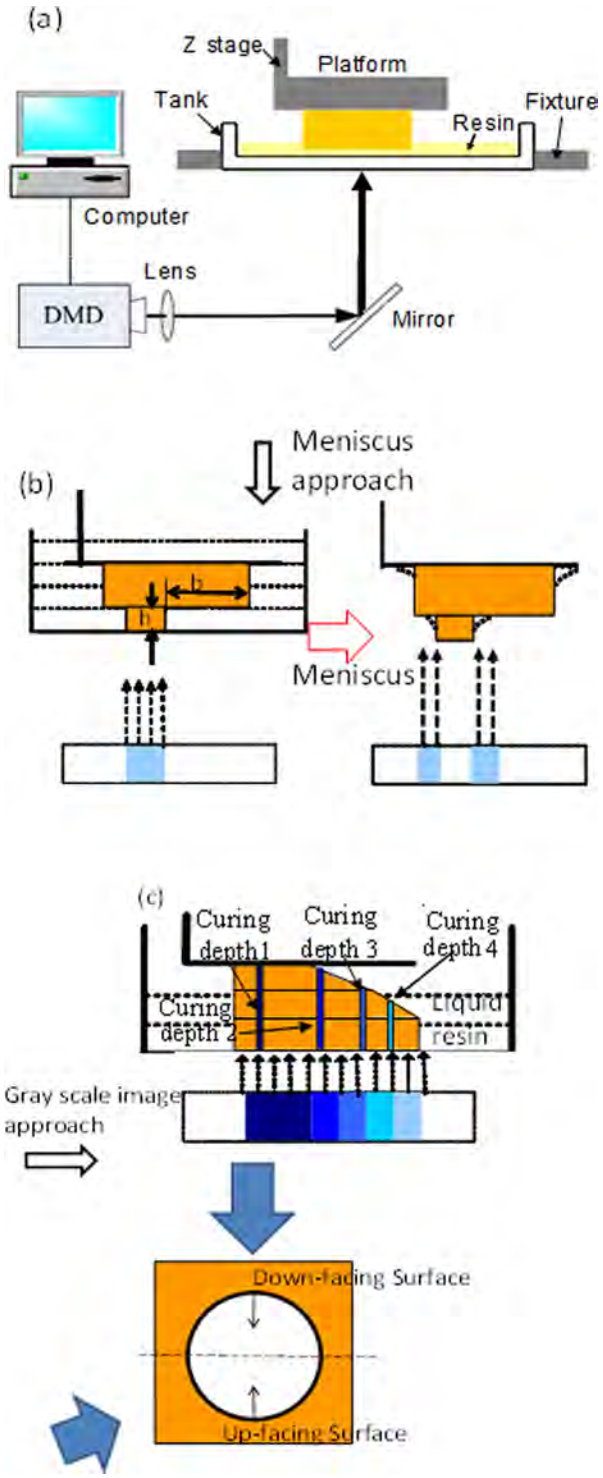

Fig. 1 Smooth surface fabrication in μSL: (*a*) an illustration of the bottom-up projection-based MIP-μSL; (*b*) a grayscale image approach for fabricating down-facing surfaces; and (*c*) a meniscus approach for fabricating up-facing surfaces

approach to the bottom-up projection-based μSL systems by considering the gravity in the meniscus modeling. In addition, the mathematical equation and related boundary conditions of the meniscus models are revised for the μSL process since all its feature dimensions are much smaller.

1.2 Down-Facing Surface. By using grayscale image values, a cure depth control approach is developed for the fabrication of smooth microscale down-facing surfaces. As shown in Fig. 1(*c*), the key idea of the grayscale image value approach is described as follows. First, a given down-facing surface can be sampled using a Z resolution that is much smaller than a layer thickness. Hence, the cure depth at each pixel can be represented by a related cure depth that has a finer resolution than the layer thickness. Accordingly, a grayscale value at each pixel can be set such that a desired energy input can be provided, which will lead to the desired cure depth at the pixel. Thus, a set of computed grayscale images can be used to fabricate smooth down-facing surfaces in the MIP-μSL process.

The remainder of the paper is organized as follows: The meniscus approach developed for the up-facing surfaces will be discussed first. Section 2 presents the models of formed meniscuses in various boundary conditions for up-facing surfaces. Accordingly, the process planning for building smooth up-facing surfaces is presented in Sec. 3. The grayscale image value approach developed for the down-facing surfaces will then be presented. Section 4 presents the models for controlling cure depths for down-facing surfaces. Accordingly, the process planning for building smooth down-facing surfaces is also discussed in the section. The experimental setup for performing physical experiments is discussed in Sec. 5. The test results for various curved surfaces including both up-facing and down-facing surfaces are presented in the section. Finally, conclusions with future work are drawn in Sec. 6.

2 Residue Meniscus Modeling for Smooth Up-Facing Surface Fabrication

2.1 Mathematical Modeling. Figure 2 shows the residue modeling in the bottom-up projection-based μSL process by considering pressure difference, surface tension, and gravitational field. Accordingly, a mathematical model can be derived from *Young–Laplace* equation (refer to Refs. [8–11])

$$\rho g y - \frac{1}{2}h_c^2 \times \frac{\rho g \ddot{y}}{(1-\sin\theta)(1+\dot{y}^2)^{2/3}} = 0 \tag{1}$$

where ρ is the density of the liquid, g is gravity acceleration, and y is the height of the meniscus above the horizontal plane surface. The contact angle θ in Eq. (1) is the angle at which the liquid resin interface meets the solidified resin surface. Specific to the given liquid and solid system, the contact angle is determined by the interactions between the liquid resin, solidified resin, and air interfaces. $\dot{y}$ and $\ddot{y}$ are the first and second derivatives of the width of the meniscus x, representatively. They represent the meniscus wetting conditions on solid substrates. h denotes the height of the vertical plane; b denotes the length of the horizontal plane; and h_c and b_0 denote the maximum values that the liquid can reach on the vertical and horizontal planes, respectively. The developed meniscus shape equation relates the curvature of the interface with gravitational influence and interfacial tension that is represented by contact angle θ and capillary height h_c. The capillary height h_c is the maximum height that the fluid can reach on an infinite vertical wall. h_c is a characteristic length for the fluid subject to gravity and surface tension.

For a specific liquid resin in the bottom-up projection-based MIP-SL system, the capillary height h_c and the maximum wetting width b_0 are fixed. To model the meniscus shape for a given feature with given b and h, five different boundary conditions are considered as follows:

(1) *Case 1*: Both $|h|$ and b can be considered as infinite. The related boundary conditions are

$$\dot{y}(x=0) = -\tan^{-1}\theta; \quad y(x=\infty) = 0 \tag{2}$$

(2) *Case 2*: $|h|$ is smaller than h_c and b is bigger than b_0. Hence, the curvature of the meniscus is decided by h. The boundary conditions are as follows:

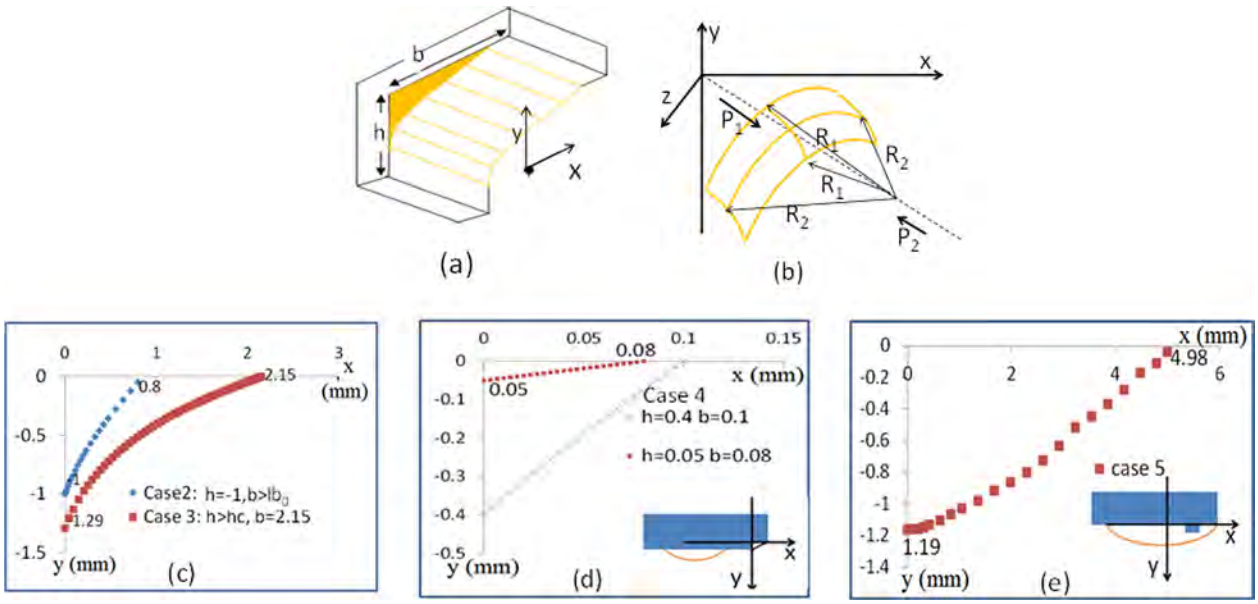

Fig. 2 Residue meniscus modeling: (*a*) meniscus wetting to intersecting plane surfaces, (*b*) fluid interface profile, and (*c*)–(*e*) plotting results of the meniscus profiles in cases 2–5

$$\dot{y}(x=0) = -\tan^{-1}\theta; \quad y(x=0) = -h$$
$$\dot{y}(y=0) \le -\tan^{-1}\left(\frac{\pi}{2} - \theta\right) \tag{3}$$

(3) *Case 3*: $|h|$ is bigger than h_c and b is smaller than b_0. Thus, the curvature of the meniscus is determined by b. The boundary conditions are as follows:

$$\dot{y}(x=0) = -\tan^{-1}\theta; \quad y(x=b) = 0$$
$$\dot{y}(y=0) \le -\tan^{-1}\left(\frac{\pi}{2} - \theta\right) \tag{4}$$

The meniscus shape can be calculated for different b and h values. Figure 2(*c*) plots the results of two examples. In an example of case 2, h equals to -1 mm and b is a value bigger than b_0. In an example of case 3, $|h|$ is bigger than h_c and b equals to 2.15 mm.

(4) *Case 4*: h is smaller than h_c and the length of the horizontal plane b is smaller than b_0. Hence, the curvature of the meniscus is decided by both b and h. The meniscus shape follows the boundary conditions

$$y(0) = -h, \quad y(b) = 0 \tag{5}$$

Case 4 is one of the two most common cases in microscale fabrication. The meniscus shape can be calculated for different b and h values. Figure 2(*d*) plots the result of two case 4 examples. In one example, h equals to -0.4 mm and b equals to 0.1 mm; in another example, h equals to -0.05 mm and b equals to 0.08 mm.

(5) *Case 5*: h is smaller than h_c and the discontinuity is connected with a horizontal plane whose size is smaller than the liquid droplet size. The problem turns into a wetting puddle in the bottom-up projection system and the boundary conditions are

$$\dot{y}(x=0) = 0, \quad y(b) = 0 \tag{6}$$

Case 5 is another case that will happen frequently in the bottom-up projection-based μSL process. Simulation software such as MATLAB can be used to solve the mathematic model of the puddle shape. Figure 2(*e*) shows the computed result of a test example, in which the bottom blocks represent the last layers of the object and a puddle is formed on the surface when moving the part out of the resin tank.

2.2 Process Parameter Calibration. Similar to our previous research [8], the contact angle θ and the capillary height h_c can be calibrated. A bottom-up projection-based MIP-μSL system is used to build test parts with intersecting horizontal and vertical surfaces. After the horizontal and vertical surfaces have been built, the part is first lifted up from the liquid resin. A liquid meniscus in contact with the intersecting surfaces will be formed on the part surfaces. After certain waiting time, the liquid volume will reach equilibrium over the horizontal wettable surface area. The part can then be moved away in the X direction to a new place, or the resin tank can be moved away from the part. A mask image is then projected on the meniscus area to cure the formed liquid resin. Note the projection image need to be planned based on the moved-up position (refer to Ref. [8]). After the meniscus shapes are cured, the built part or the resin tank is moved back to continue the building process. For the liquid resins used in our experiments (Perfactory SI500 from *EnvisionTEC*, Ferndale, MI), it is estimated that $\theta = 25$ deg and $h_c = 1.88$ mm. Another liquid resin, E-Shell also from *EnvisionTEC*, is measured with θ and h_c as 21 deg and 1.72 mm, respectively. Table 1 shows the material

Table 1 Residue modeling parameters

Property	E-shell (bottom-up)	SI 500 (bottom-up)	SI 500 (top-down)
Viscosity (cP)	339.8	180	180
Density (g/cm^3)	1.19	1.10	1.10
Contact angle (deg)	21	25	25
Capillary height (mm)	1.72	1.88	1.40
Maximum wetting (b_0) (mm)	2.25	1.567	2.5

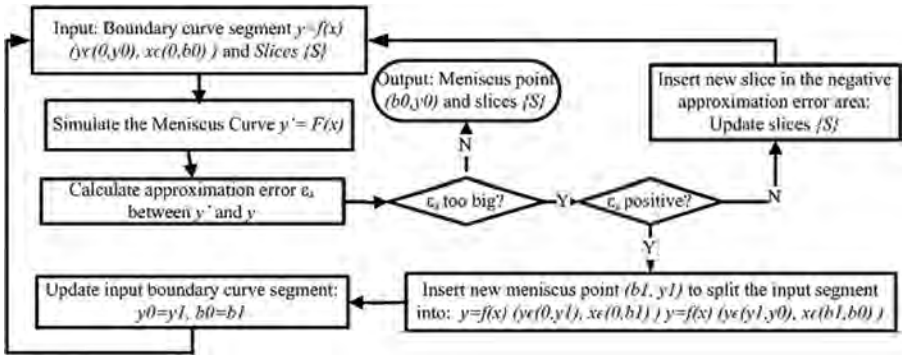

Fig. 3 The framework of the algorithm for generating the minimum meniscus points and the slices with the least dipping number and acceptable approximation error

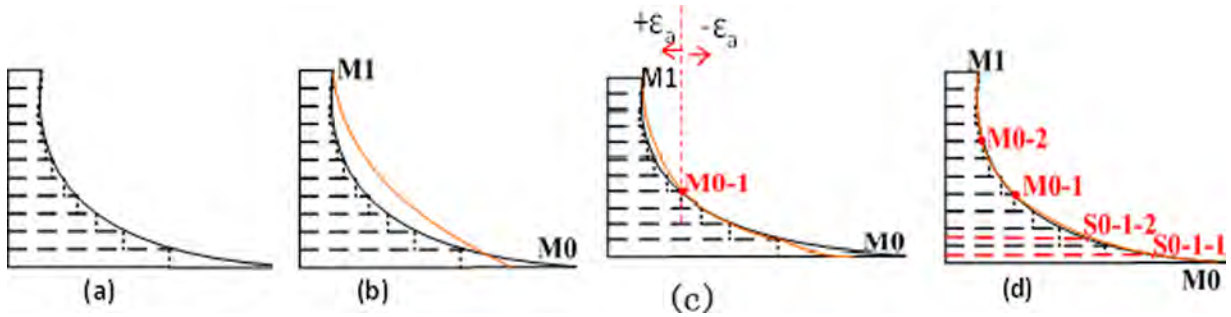

Fig. 4 An illustration of meniscus process optimization

properties and measurements of model parameters of these two materials.

3 Optimization of Meniscus Process Parameters

Suppose a boundary curve $y=f(x)$ $(y \in (0, y_0),\ x \in (0, b_0))$ is given, where y_0 and b_0 are initial values of the sizes of the given boundary curve, and y_0 is smaller than the maximum vertical height h_c as discussed in the meniscus model. An algorithm based on the greedy heuristic can be developed as shown in Fig. 3. Note that we try to find a minimum number of meniscus forming operations for building a given CAD model. As shown in our test cases (refer to Sec. 5.2), only 2–3 such operations are required for forming desired meniscuses. This is very different from the previous approach [12], in which the formed meniscuses are cured in each layer. Due to a large number of interruptions (same as the layer number), the part building process based on Ref. [12] will be very slow.

Figure 4 shows an example based on the presented algorithm. The meniscus shape in the area of $y \in (0, y_0)$ is first estimated and compared with the input geometry. As shown in Fig. 4(*b*), the meniscus curve of the given feature is simulated (refer to the gray curve). The given CAD model profile is shown in the black curve. The shape error ε_a can be computed by comparing the two curves. If ε_a is within the acceptable shape error range, M_0 and M_1 can be selected as the planned meniscus points. Otherwise, two strategies will be applied based on the approximation errors: (1) If the meniscus curve is outside the CAD profile (i.e., a positive ε_a is computed), the point at which the biggest approximation error occurs will be selected as an additional meniscus point (refer to $M_{0\text{-}1}$ in Fig. 4(*c*)) and (2) If the meniscus curve is inside the CAD profile (i.e., a negative ε_a is computed), new slices will be added in the building process to push the meniscus curve outward to better approximate the given profile. For example, for the gray curve between M_{0-1} and M_0 in Fig. 4(*c*), two additional slices *S*0-1-1 and *S*0-1-2 are added such that the simulated meniscus curves can better approximate the CAD profile.

Based on the updated meniscus points and slices, the new meniscus profile and the corresponding approximation error are recalculated. Such process is iterated until the approximation error is within a defined satisfactory range. Related meniscus forming operations can be planned based on the computed meniscus points. In addition, a set of mask projection images (i.e., $\text{image}_{\text{part}}$ and $\text{image}_{\text{meniscus}}$) can be computed for the building process. Accordingly, $\text{image}_{\text{part}}$ will be used in solidifying resin in each layer. When the current layer comes to the meniscus point M_{hi} related to h_i, the fabricated model will be raised out of liquid resin. After a certain waiting time, the tank will be moved away and the related mask image ($\text{image}_{\text{meniscus}}$) is projected on part surfaces to form desired meniscus shapes in such areas.

3.1 Approaches for Modifying Meniscus Profile. The following algorithm is used for determining whether a meniscus profile needs to be refined based on the computed approximation error, and accordingly what strategy is used to modify the meniscus profile:

Algorithm 1.

Input: A segment of curve surface f(x, h) and a layer thickness.
Find: A set of b_i and h_i
Satisfy: $F_i(x) = F(b_i, h_i)$
Calculate:
$\varepsilon_{a\_i} = \int_{x_i}^{x_{i+1}} (f(x) - F_I(x))dx \approx \sum_{k=0}^{k=m} \nabla d_i$
$\varepsilon_a = \sum_{i=0}^{i=n} \varepsilon_{a\_i}$
if $\varepsilon_a < -\varepsilon_{\max}$, use Algorithm 1.1 to plan new slice images.
if $\varepsilon_a > \varepsilon_{\max}$, use Algorithm 1.2 to plan new meniscus points.
End.

3.2 New Slice Planning for Negative Approximation Error. As shown in Fig. 5, the solid curves represent the given CAD model profile and the dotted curves represent the formed meniscus profile. For the two slices as shown in Fig. 5(*a*), there is

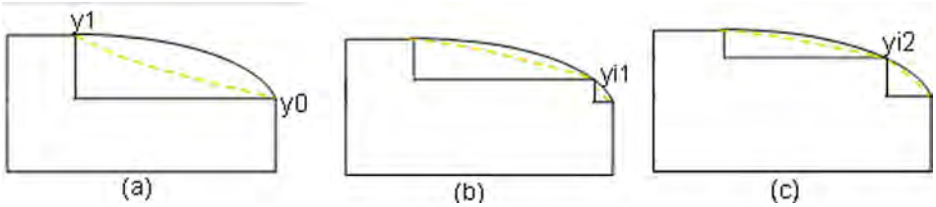

Fig. 5 An illustration of influence of new slice planning on formed meniscus shape

a negative approximation error since the simulated meniscus curve is inside the given CAD model profile. By inserting a new slicing plane between the two slices (refer to the two examples as shown in Figs. 5(*b*) and 5(*c*)), the formed meniscuses will change their shapes due to the inserted slice layer. In addition, inserting the additional slices at different positions will lead to different meniscus shapes. Accordingly, a simple algorithm (Algorithm 1.1) can be used to identify the additional slices that can achieve the minimum approximation error.

Algorithm 1.1.

Input: The segment of curve surface f(x, y) ($y_0 < y < y_1$) which gives negative approximation errors. A set of y_i is sampled from the range of y_0 and y_1 and used as the candidates for inserting slices.
Find: A slice position y_s
Calculate:
Simulate the meniscus model for each y_i;
Compute $\{\varepsilon_{a\_yi}\}$ using the shape error algorithm as described in Algorithm 1;
Output y_s that gives the smallest $|\varepsilon_{a\_yi}|$.
End.

Based on the computed additional slicing positions y_s, the input CAD model is sliced at the position $y = y\_s$. The sliced mask image is then added into the mask projection image set $\{S\}$ for the layer-based building process. Note that the fabricated part may have nonuniform layer thickness in order to achieve more accurate meniscus profile.

3.3 New Meniscus Point Planning for Positive Approximation Error. As shown in Fig. 6(*a*), the solid black curves represent the CAD model profile and the dotted lines are the sliced layers. The meniscus is then formed after it reaches the layer of M_1. The formed meniscus is represented by the gray curve as shown in Fig. 6(*b*). The formed meniscus between M_0 and M_1 is outside the CAD profile, which leads to positive approximation errors. Instead of forming the meniscus shape until the part is built to the layer M_1, two or more meniscus points can be added between M_0 and M_1 to form meniscus shapes with less approximation error. As shown in Fig. 6(*c*), when inserting a meniscus point at the layer of M_{0-1}, the formed meniscuses between the portions of M_0M_{0-1} and $M_{0-1}M_1$ can have a smaller approximation error.

Algorithm 1.2.

Input: The segment of curve surface f(x, y) ($M_0 < y < M_1$) which gives positive approximation errors. A set of y_i ($i = 1,2,.,m$) are sampled from the range of M_0 and M_1, and are the candidates for inserting sub-meniscus positions.
Find: A sub-meniscus position y_d.
Calculate:
Simulate the meniscus model for each y_i;
Compute $\{\varepsilon_{a\_yi}\}$ using the shape error algorithm as described in Algorithm 1;
Output y_d that gives the smallest $|\varepsilon_{a\_yi}|$.
End.

Based on the computed meniscus point positions y_d that need to be inserted, we will stop the building process when the built layers reach y_d. The meniscus related to the previous portion (i.e., between M_0 and M_{0-1} as shown in Fig. 6(*c*)) will be formed and cured. Then the layer-based building process will continue until it reaches the next meniscus point (i.e., M_1). Accordingly, the meniscus related to the portion between M_{0-1} and M_1 (refer to Fig. 6(*c*)) can be formed. Hence, the fabricated part with the planned meniscus shapes will have smaller approximation error compared to the part that is built with a single meniscus point (refer to Fig. 6(*b*)). A tradeoff to make is that the building process would be longer due to an additional meniscus point and related meniscus forming process.

4 Cure Depth Modeling for Down-Facing Surface Fabrication

The meniscus equilibrium method can only address the fabrication of up-facing surfaces. To improve the surface finish of down-facing surfaces, a method by using grayscale mask image values to achieve controlled cure depths has been developed for the MIP-μSL. The method was motivated by the parameter estimation method that was developed for the scanning-based SL process [13].

4.1 Modeling Cure Depths Related to Grayscale Image Values. As studied in both scanning-based and projection-based SL processes [14,15], the critical threshold (E_c) is a primary parameter for a given photosensitive resin. Liquid resin will be solidified when the exposed energy is bigger than E_c; otherwise, the resin will remain as liquid or gel that will be washed off. In addition, the cure depth (C_d) is directly related to the energy input

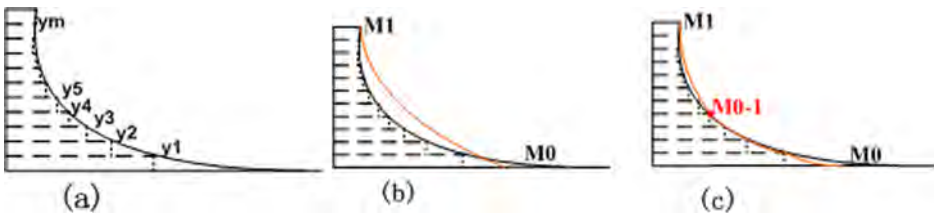

Fig. 6 An illustration of influence of submeniscus points on the formed meniscus shape

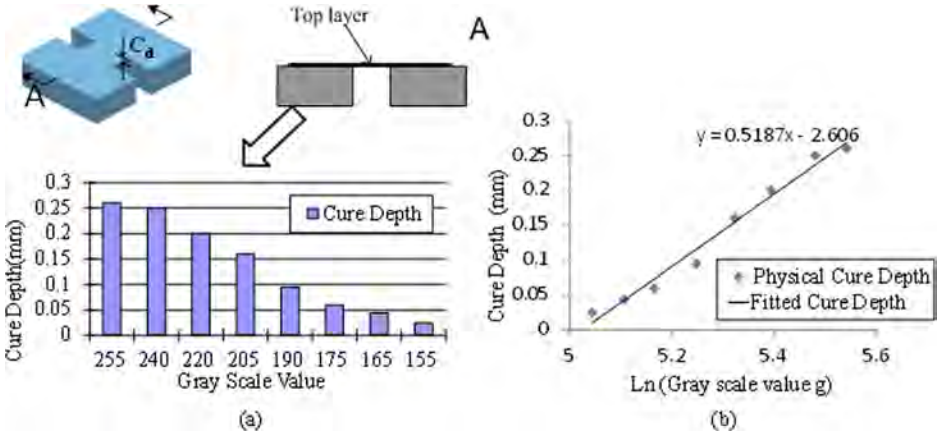

Fig. 7 Relation between the cure depth and the grayscale value: (*a*) experiments on C_d and g values and (*b*) relation of C_d and ln(g) values

E if $E > E_c$. The dependence of C_d as a function of the exposure E is generally log-linear [12]. That is, their relation can be described using the following equation:

$$C_d = D_p \ln\left(\frac{E}{E_c}\right) \tag{7}$$

One way to control E is to adjust the exposure time for a binary projection image [16]. Another approach is to adjust pixels' grayscale values while fixing the exposure time of the projection image. In comparison, the approach of varying grayscale image values is easier to control since the projection time for the whole image is fixed. In our MIP-μSL process, the full light intensity is projected to an image pixel if its grayscale value $g = 255$; however, when $0 < g < 255$, only partial light intensity will be projected for curing the resin area related to the pixel.

Corresponding to a given E_c and an exposure time T, a threshold grayscale value g_c can be identified. Experiments have been performed to calibrate the relations between the cure depth and the grayscale values. Figure 7(*a*) shows the CAD model of a designed part for the calibration study. In the test, the exposure time was set at 10 s. A set of mask images with different grayscale values are used to cure the top layer. The built part is then taken out and cleaned. The cured layer thickness C_d of the top layer was measured under microscope. The recorded C_d values for different grayscale values are shown in Fig. 7(*a*). The cure depth increases with the set grayscale value. In addition, the grayscale value threshold g_c is around 100 when $T = 10$ s. For a pixel with $g < g_c$, liquid resin is not cured or the cure depth is too small for a given layer thickness (0.01–0.02 mm is used in our setup). Figure 7(*b*) shows the relation between C_d and ln(g). The relation can be approximated by the following equation, which matches Eq. (7) well:

$$F(x) = \begin{cases} 0.5187 \times \ln(g) - 2.606, & g \geq g_c \\ 0, & g < g_c \end{cases} \tag{8}$$

Hence, by changing the grayscale values of neighboring pixels in a projected mask image, the cure depth related to the pixels can be gradually changed (smaller than a layer thickness). Thus, a higher Z resolution of down-facing surfaces can be achieved to improve their surface finish. In the process planning for a given 3D model with down-facing surfaces, the cure depth at each pixel needs to be controlled by adjusting its grayscale value. In addition, an upward Z offsetting distance needs to be considered since the Z over-cure between the layers is required in the layer-based fabrication process.

4.2 Process Planning and Cure Depth Control for Down-Facing Surfaces. A schematic illustration of the traditional slicing and the grayscale image planning methods is shown in Fig. 8(*a*). In the traditional slicing method, a set of layers are

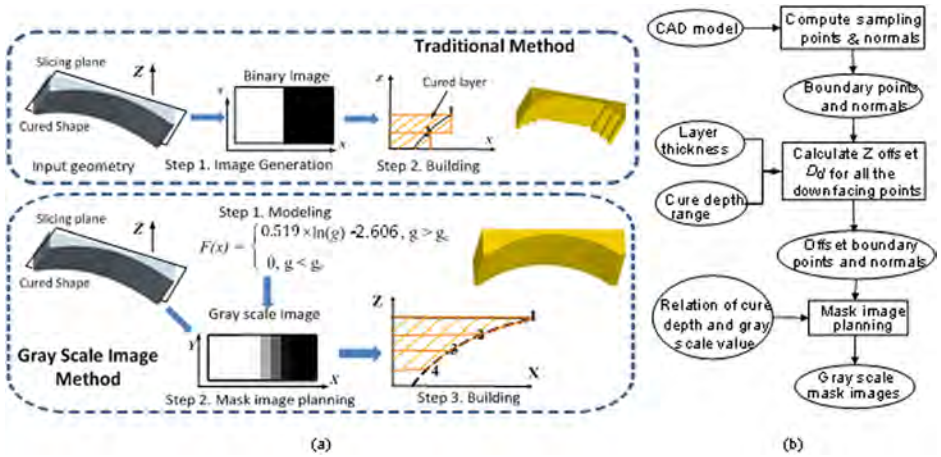

Fig. 8 The grayscale image planning method and an image generation algorithm: (*a*) comparison between the traditional method and grayscale image method and (*b*) grayscale image generation algorithm

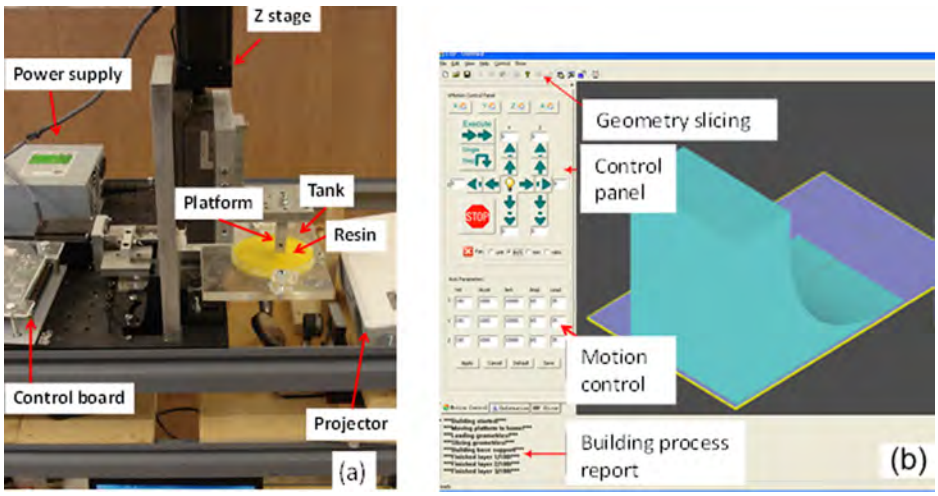

Fig. 9 The developed MIP-SL testbed for fabricating smooth surfaces: (*a*) hardware setup and (*b*) software system

computed based on a set of Z slicing planes. Accordingly, a binary mask image is generated for each slicing plane. It will be used in the MIP-μSL process for building the layer. In comparison, in the grayscale image planning method, we first calculate the Z thickness of each pixel based on the layered depth-normal image representation [17]. The Z thickness at each pixel is then converted into grayscale values of a related mask image based on the minimum and maximum cure depths (e.g., 0.05 mm and 0.25 mm, respectively, in our setup). Note that the Z offsetting to address the layer over-cure needs to be considered in the step. Based on the Z offsetting result, the desired cure depth in each layer is bigger than the minimum achievable cure depth and smaller than the maximum achievable cure depth. Accordingly, the established relation between cure depth and the grayscale values can be used to set the mask images with desired grayscale values. When building the related layers, such planned mask images will lead to smoother down-facing surfaces in the MIP-μSL process.

Figure 8(*b*) shows a related algorithm for the planning of grayscale mask images based on an input CAD model.

5 Fabrication of Microscale Smooth Surfaces

5.1 Experimental Setup. A prototype system has been built for verifying the presented methods. The hardware setup of the developed bottom-up based MIP-μSL system is shown in Fig. 9(*a*). A modified projector (Acer H5360) with a TI's digital micromirror device (DMD) chip is used as the projection device. The DMD resolution is 1024×768 and the envelope size is set at 12.7×9.5 mm. A linear stage from Aerotech, Inc. (Pittsburgh, PA) with 1 μm resolution is used as an elevator in the Z axis. The layer thickness is set between 10 and 20 μm. A linear stage from Servo Systems Co. (Montville, NJ) is used to drive the tank in the X axis. A four-axis motion controller with 28 bidirectional I/O pins is used to drive the linear stages and to synchronize the movement and projection.

A process control testbed has been developed using C++ language, as shown in Fig. 9(*b*). A MATLAB program is used to simulate the meniscus shapes. The developed software system performs geometry slicing and generates the layer projection and meniscus images.

5.2 Results and Discussion on Microscale Up-Facing Surface Fabrication

5.2.1 Tests on Concave Surfaces. As shown in Fig. 10, a CAD model ($3.81 \times 3.81 \times 6.35$ mm) with a concave surface was used in the test. The traditional layer-based MIP-μSL process, which is denoted as $M1$, was used to build the part. The layer thickness was set as 20 μm. Figures 10(*a*), 10(*e*), and 10(*h*) show the microscopic images of the area A_1 and A_2 portions of the built part. As shown in Figs. 10(*e*) and 10(*h*), although a small thickness was applied, the layer stepping effect is still visible.

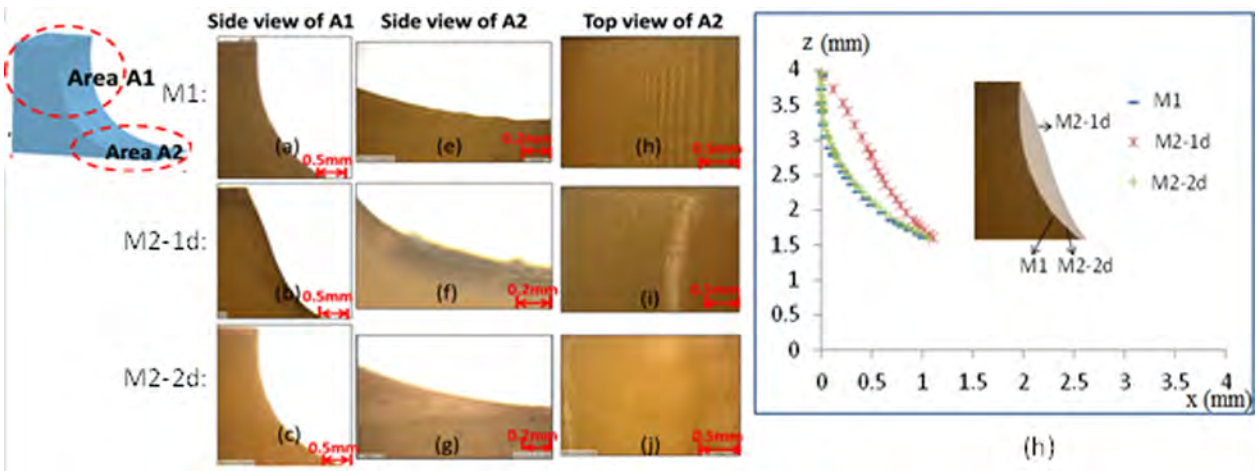

Fig. 10 A test case of concave surface

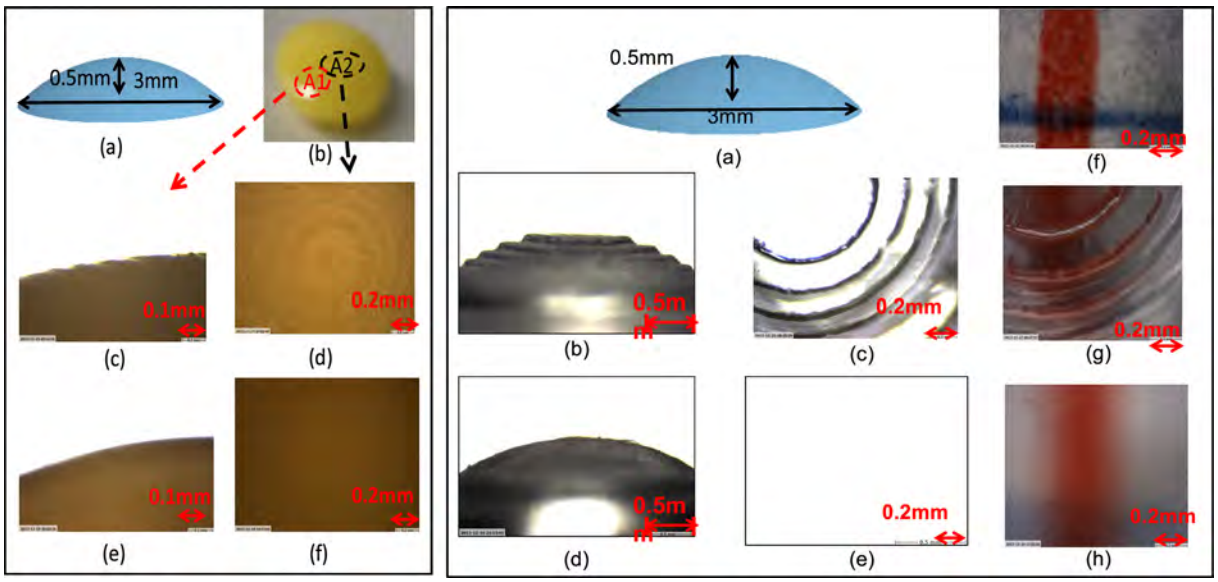

Fig. 11 A test case of a microlens using: SI-500 (left panel)—(*a*) CAD model, (*b*) physical model, (*c*) side view A_1—part A, (*d*) top view A_2—part A, (*e*) side view A_1—part B, and (*f*) top view A_2—part B; and E-Shell (right panel)—(*a*) CAD model, (*b*) side view—lens A, (*c*) top view—lens A, (*d*) side view—lens B, (*e*) top view—lens B, (*f*) paper for test, (*g*) view of paper under lens A, and (*h*) view of paper under lens B

A one-time dipping meniscus method, which is denoted as *M*2-1 *d*, was used to fabricate the same CAD model. The microscopic images of the same two areas A_1 and A_2 of the fabricated part are shown in Figs. 10(*b*), 10(*f*), and 10(*i*). Although the surface finish is improved, the one-time dipping meniscus method brings a large approximation error as shown in Figs. 10(*b*) and 10(*f*).

To reduce the approximation error, a controlled meniscus method with two-dipping meniscus points (denoted as *M*2-2 *d*) was used to fabricate the same CAD model. The microscopic images of the same two areas A_1 and A_2 of the fabricated result are shown in Figs. 10(*c*), 10(*g*), and 10(*j*). Based on the method as discussed in Sec. 3.3, the fabricated part profile is smooth and closely approximates the input CAD model profile.

5.2.2 Tests on Convex Surfaces. Figure 11 shows the fabrication results of a microlens with a convex surface ($2.54 \times 2.54 \times 0.5$ mm) using two types of resins: SI500 and E-shell. The fabrication results using SI500 are shown in the left panel of Fig. 11. Figures 11(*a*) and 11(*b*) on the left panel show the CAD model of the microlens and a related physical object using SI500, respectively. Figures 11(*c*) and 11(*d*) on the left panel are the microscopic images of area A_1 and A_2 of the part fabricated by the traditional layer-based MIP-μSL process. Figures 11(*e*) and 11(*f*) on the left panel are the microscopic images of the part fabricated by the meniscus method.

A transparent resin, E-shell, was used to fabricate the same microlens. The fabrication results based on E-shell are shown in the right panel of Fig. 11. In order to demonstrate the effectiveness of our method, a large layer thickness (100 μm) is used in the fabrication process. The fabricated microlenses using the traditional layer-based MIP-μSL process and the meniscus approach are denoted as lenses A and B in the right panel of Fig. 11, respectively. As shown in Fig. 11(*f*) of the right panel, a paper with a blue and red line was used to test the fabricated microlenses. Figure 11(*g*), on the right panel, shows the optical performance of lens A. The paper image is distorted by the microlens' rough surface due to the stair-stepping effect. In comparison, the optical performance of lens B on the same paper is shown in Fig. 11(*h*) of the right panel, which demonstrates a significant improvement over that of lens A.

5.2.3 Quantitative Study of Test Cases. Quantitative measurements have been performed to better understand the surface quality improvement. A precision measurement machine (Sol from Micro Vu, Inc., Windsor, CA) is used to record the surface profiles of the fabricated microstructures:

• *Approximation errors.* The profiles of area A_1 of the three built parts as showed in Fig. 10 are sampled and plotted in Fig. 10(*k*). Because the surfaces in area A_1 are close to be vertical surfaces (i.e., $N \cdot Z \approx 0$ for the surface normal N and the Z axis), there is no obvious staircase effect in this area for all the three parts. However, for the surfaces in area A_2 that are close to be flat surfaces, obvious staircase effect exists for part *M*1 as shown in Fig. 10(*h*). For part *M*2-1 *d*, the one-dipping meniscus method leaves a large amount of extra resin in its meniscus area. Consequently, a big approximation error exists. By inserting an additional meniscus point using the algorithm described in Sec. 3, the part *M*2-2 *d* using a two-dipping meniscus method is much closer to the original model. Table 2 shows the statistics of the approximation errors for the three fabricated parts.

• *Surface roughness.* For concave surfaces, the profile of area A_2 of the built part using the traditional MIP-μSL process (refer to Fig. 10(*e*)) is shown in Fig. 12(*a*). In comparison, the same area of the built part using the two-dipping meniscus method (refer to Fig. 10(*g*)) is also showed in Fig. 12(*a*). For convex surfaces, the profiles of part A built by the traditional MIP-μSL process (refer to Fig. 11(*c*) on the left panel) and part B built by the meniscus method (refer to Fig. 11(*e*) on the left panel) are plotted in Fig. 12(*b*).

Table 3 shows the measurement results of the parts as shown in Figs. 10 and 11. The measured roughness verifies the

Table 2 Accuracy of the built geometries with different building strategies

	Accuracy (μm)	
Fabricated parts	Maximum distance	Average distance
Figure 10—*M*1	12	4
Figure 10—*M*2-2*d*	6	2.3
Figure 10—*M*2-1*d*	375	258
CAD model	0	0

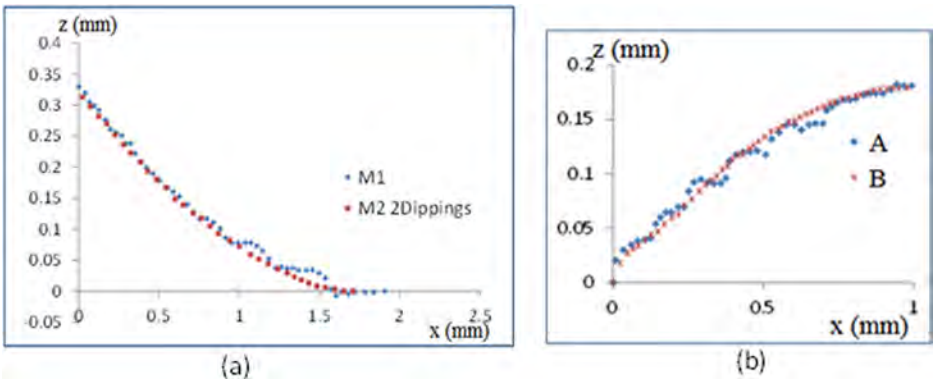

Fig. 12 Surface measurement results: (*a*) area A_2 of parts in Fig. 10 and (*b*) parts A and B in Figs. 11(*c*) and 11(*e*) of the left panel

Table 3 Roughness of the built surfaces in Figs. 10–11

Surface	Roughness measures (mm)		
	R_a	R_q	R_z
Figure 10—M_1	0.0067	0.0088	0.016
Figure 10—M_2-two dippings	0.0007	0.0009	0.0017
Figure 11 (left panel)—A	0.0037	0.0044	0.0072
Figure 11 (left panel)—B	0.0007	0.0011	0.0022

effectiveness of the controlled-meniscus-based approach in improving the surface finish of both concave and convex up-facing surfaces.

5.3 Results and Discussion on Microscale Down-Facing Surface Fabrication. The controlled cure depth method, as discussed in Sec. 4, is used to test the down-facing surface fabrication in the MIP-μSL process. Figure 13(*a*) shows a CAD model with a curved down-facing surface. The X, Y, and Z dimensions of the part are $10 \times 6.7 \times 5.26$ mm, respectively. In order to better demonstrate the fabrication difference between the layer-based and grayscale image-based methods, a relatively large layer thickness (0.075 mm) is used to build the CAD model. Figure 13(*b*) shows a fabricated part using resin SI500. Two surface areas of the parts (A and B) are highlighted. Both the layer-based and grayscale image-based methods are used to build the part. The same process parameters such as projection time, material, layer thickness, and moving parameters are used in the building process. The only difference is that one part is fabricated with the proposed grayscale image approach while another one is built without the approach. Hence, the planned mask projection images are different. Figures 13(*c*) and 13(*e*) are the microscopic images of areas A and B of the part fabricated using the traditional approach (denoted as $M1$). In comparison, Figs. 13(*d*) and 13(*f*) show the two areas using the proposed grayscale image approach (denoted as $M2$).

Figure 13(*g*) shows the measured surface profiles of the two parts fabricated by $M1$ and $M2$. It demonstrates that the traditional slicing-plane-based mask image planning method will lead to Z over-cure and stair-stepping problems in the MIP-μSL process.

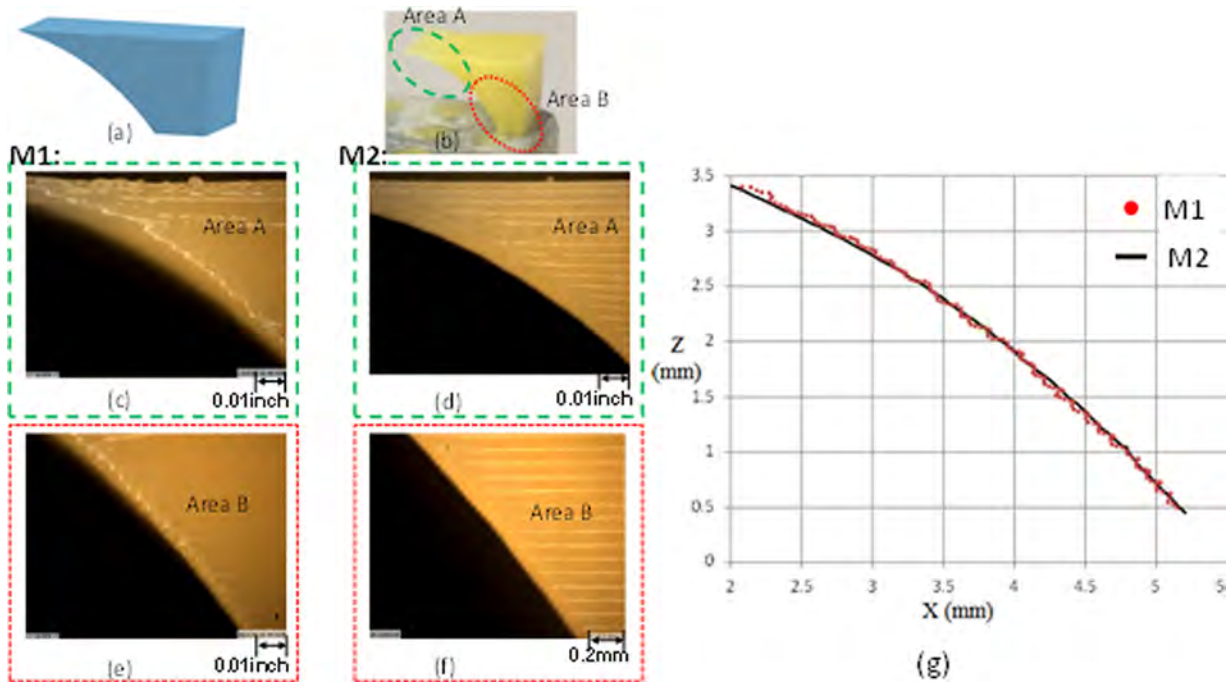

Fig. 13 Down-facing surface fabrication using different methods

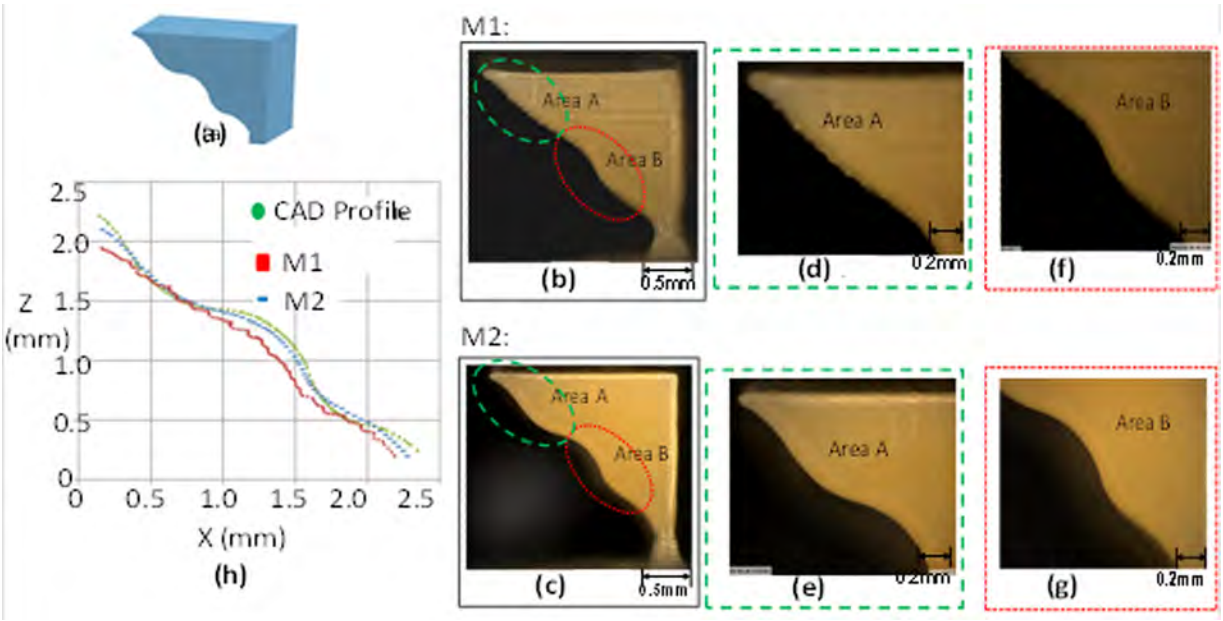

Fig. 14 Built down-facing surfaces using different mask image planning methods

By accurately controlling the cure depths through the grayscale image planning method, both the Z over-cure and stair-stepping problems can be effectively addressed. Therefore, the surface quality and geometry accuracy of down-facing surfaces can be significantly improved.

To further verify the effectiveness of the proposed grayscale image planning method, another test case with a waved down-facing surface is tested. Figure 14(*a*) shows the CAD model of the test case. The X, Y, and Z dimensions of the model are $3.5 \times 2.5 \times 2.185$ mm, respectively. The part is fabricated using the same process parameters except different mask projection images. A layer thickness of 0.070 mm is used in both test cases. Figure 14(*b*) shows the fabricated part using the slicing-plane-based mask image planning method ($M1$). Figure 14(*c*) shows the fabricated part using the grayscale image planning method ($M2$). The microscopic images of two different areas (A and B) in the fabricated parts are shown in Figs. 14(*d*)–14(*g*). Figure 14(*h*) shows the measured surface profiles of the two fabricated parts. In Fig. 14(*h*), the dotted line represents the CAD profile, the square line represents the profile of the fabricated part using $M1$, and the dashed line represents the profile of the fabricated part using $M2$. Compared to the part based on $M1$, the part built with $M2$ has much better surface finish and smaller Z over-cure error. The two test cases verify the grayscale mask image method is able to control the cure depth in the MIP-μSL process and improve the surface quality of down-facing surfaces.

6 Conclusions

A novel smooth surface fabrication method has been presented for the bottom-up projection-based MIP-μSL process. (1) For fabricating smooth up-facing surfaces, an approach based on forming controlled meniscus shape on microscopic 2D layers has been presented. Meniscus modeling by considering various boundary conditions has been developed. Accordingly, a process planning problem has been formulated for identifying the minimum number of meniscus points with satisfactory approximation errors. A heuristic-based algorithm has also been presented for the formulated optimization problem. (2) For fabricating smooth down-facing surfaces, a grayscale image planning method has been developed to accurately control the energy input of each pixel. A relationship between the cure depth and the grayscale values of a projection image has been calibrated and established. Accordingly, an image planning algorithm has been developed for computing the grayscale values of each pixel such that the fabricated object can closely approximate the given CAD model.

An MIP-μSL testbed with both hardware and software systems was constructed to verify the proposed meniscus and grayscale image approaches for fabricating smooth up-facing and down-facing surfaces, respectively. Designed experiments using the developed testbed have been performed to compare different fabrication methods in the MIP-μSL process. The experimental results have illustrated the effectiveness of the presented methods in improving the surface finish of both up-facing and down-facing surfaces in the bottom-up projection-based MIP-μSL process. Hence, a given part could be fabricated by classifying its curved surfaces into up-facing and down-facing regions and accordingly using the corresponding approach. The current development could be improved in many avenues including: (1) exploring more advanced optimization algorithms to determine process parameters such as slicing parameters and meniscus points to minimize approximation errors; (2) investigating meniscus forming approaches for liquid resin and slurry that may have much higher viscosities; (3) developing advanced algorithm for parts with complex shapes to determine the meniscus curing region, grayscale image curing region and regular region automatically and efficiently; and (4) integrating the developed process planning and optimization algorithms to optimize the fabrication process for given parts.

Acknowledgment

The authors acknowledge the support of National Science Foundation Grant No. NSF-CMMI 1151191.

References

[1] Cheng, Y.-L., and Lee, M.-L., 2009, "Development of Dynamic Masking Rapid Prototyping System for Application in Tissue Engineering," Rapid Prototyping J., **15**(1), pp. 29–41.

[2] Choi, J. W., Ha, Y. M., Lee, S. H., and Choi, K. H., 2006, "Design of Microstereolithography System Based on Dynamic Image Projection for Fabrication of Three-Dimensional Microstructures," J. Mech. Sci. Technol., **20**(12), pp. 2094–2104.

[3] Choi, J.-W., Wicker, R., Lee, S.-H., Choi, K.-H., Ha, C.-S., and Chung, I., 2009, "Fabrication of 3D Biocompatible/Biodegradable Micro-Scaffolds Using Dynamic Mask Projection Microstereolithography," J. Mater. Process. Technol., **209**(15), pp. 5494–5503.

[4] Park, I. B., Ha, Y. M., and Lee, S. H., 2011, "Dithering Method for Improving the Surface Quality of a Microstructure in Projection Microstereolithography," Int. J. Adv. Manuf. Technol., **52**(5–8), pp. 545–553.
[5] Sun, C., Fang, N., Wu, D. M., and Zhang, X., 2005, "Projection Micro-Stereolithography Using Digital Micro-Mirror Dynamic Mask," Sens. Actuators, A, **121**(1), pp. 113–120.
[6] Ha, Y. M., Choi, J. W., and Lee, S. H., 2008, "Mass Production of 3-D Microstructures Using Projection Microstereolithography," J. Mech. Sci. Technol., **22**(3), pp. 514–521.
[7] Gandhi, P., and Bhole, K., 2013, "Characterization of 'Bulk Lithography' Process for Fabrication of Three-Dimensional Microstructures," ASME J. Micro Nano-Manuf., **1**(4), p. 041002.
[8] Pan, Y., Zhao, X., Zhou, C., and Chen, Y., 2012, "Smooth Surface Fabrication in Mask Projection Based Stereolithography," J. Manuf. Processes, **14**(4), pp. 460–470.
[9] Wayner, P. C., 1980, "Interfacial Profile in the Contact Line Region of a Finite Contact Angle System," J. Colloid Interface Sci., **77**(2), pp. 495–500.
[10] White, L. R., 1977, "On Deviations From Young's Equation," J. Chem. Soc., Faraday Trans. 1, **73**(1), pp. 390–398.
[11] Jairazbhoy, V., 1997, "Prediction of Equilibrium Shapes and Pedestal Heights of Solder Joints for Leadless Chip Components," Microelectron. Reliab., **37**(8), pp. 1276–1276.
[12] Narahara, H., and Saito, K., 1995, "Study on the Improvement of Surface Roughness of Complex Model Created by Three Dimensional Photofabrication (1st Report) Proposal of Lift Up Irradiation Method," J. Jpn. Soc. Precis. Eng., **61**(2), pp. 233–233.
[13] Sager, B., and Rosen, D. W., 2008, "Use of Parameter Estimation for Stereolithography Surface Finish Improvement," Rapid Prototyping J., **14**(4), pp. 213–220.
[14] Zhou, C., Chen, Y., and Waltz, R. A., 2009, "Optimized Mask Image Projection for Solid Freeform Fabrication," ASME J. Manuf. Sci. Eng., **131**(6), p. 061004.
[15] Paul, F. J., 1992, *Rapid Prototyping and Manufacturing, Fundamentals of Stereolithography*, SME, Dearborn, MI, pp. 135–141.
[16] Limaye, A. S., and Rosen, D. W., 2007, "Process Planning Method for Mask Projection Micro-Stereolithography," Rapid Prototyping J., **13**(2), pp. 76–84.
[17] Wang, C. C. L., Leung, Y.-S., and Chen, Y., 2010, "Solid Modeling of Polyhedral Objects by Layered Depth-Normal Images on the GPU," Comput.-Aided Des., **42**(6), pp. 535–544.